Carbon Nanotubes by a CVD Method. Part II: Formation of Nanotubes from (Mg, Fe)O Catalysts

Pierre Coquay,[†] **Alain Peigney,**[‡] **Eddy De Grave,**[†] **Robert E. Vandenberghe,**[†] **and Christophe Laurent*,**[‡]

NUMAT, Department of Subatomic and Radiation Physics, University of Ghent, Proeftuinstraat 86, B-9000 Gent, Belgium, and CIRIMAT UMR CNRS 5085/LCMIE, Centre Interuniversitaire de Recherche et d'Ingénierie des Matériaux, Université Paul-Sabatier, 31062 Toulouse Cedex 4, France

The aim of this paper is to study the formation of carbon nanotubes (CNTs) from different Fe/MgO oxide powders that were prepared by combustion synthesis and characterized in detail in a companion paper. Depending on the synthesis conditions, several iron species are present in the starting oxides including Fe^{2+} ions, octahedral Fe^{3+} ions, Fe^{3+} clusters, and $MgFe_2O_4$-like nanoparticles. Upon reduction during heating at 5 °C/min up to 1000 °C in H_2/CH_4 of the oxide powders, the octahedral Fe^{3+} ions tend to form Fe^{2+} ions, which are not likely to be reduced to metallic iron whereas the $MgFe_2O_4$-like particles are directly reduced to metallic iron. The reduced phases are α-Fe, Fe_3C, and γ-Fe−C. Fe_3C appears as the postreaction phase involved in the formation of carbon filaments (CNTs and thick carbon nanofibers). Thick carbon nanofibers are formed from catalyst particles originating from poorly dispersed species (Fe^{3+} clusters and $MgFe_2O_4$-like particles). The nanofiber outer diameter is determined by the particle size. The reduction of the iron ions and clusters that are well dispersed in the MgO lattice leads to small catalytic particles (<5 nm), which tend to form SWNTS and DWNTs with an inner diameter close to 2 nm. Well-dispersed $MgFe_2O_4$-like particles can also be reduced to small metal particles with a narrow size distribution, producing SWNTs and DWNTs. The present results will help in tailoring oxide precursors for the controlled formation of CNTs.

Introduction

Chemical methods known as catalytic chemical vapor deposition (CCVD) are widely used for the synthesis of carbon nanotubes (CNTs) owing to several features, including their great potential for the production of large quantities at low cost and the possibility to form the CNTs either very locally or inside a host material. These methods, similar to those used for several decades for the synthesis of various filamentous forms of carbon, involve the catalytic decomposition of a carbonaceous gas (hydrocarbon or carbon monoxide) on transition-metal nanometric particles. Although several mechanisms do exist, CNTs are mainly produced by catalyst particles below ca. 3 nm in diameter.[1−4] It is thus important to tailor the precursor so that the catalyst particles retain a small size and indeed are active for CNT formation under given experimental conditions (nature of carbon source, temperature, dwell time, heating/cooling rates). However, relatively few articles report detailed studies on the starting material.[5−7] We have proposed an original CCVD method[8] using oxide solid solutions as the starting materials. Indeed, the reduction in a H_2/CH_4 atmosphere of α-$Al_{1.9}Fe_{0.1}O_3$, in which the ferric ions are well dispersed, produces pristine Fe nanoparticles at a temperature high enough for them to catalyze the decomposition of CH_4 and the in situ formation of CNTs including single-walled CNTs (SWNTs).[8] Several characteristics of the starting alumina-based oxide including its iron content,[9] crystallographic form,[10] and specific surface area[11]

have been investigated in order to increase the proportion of single-walled CNTs (SWNTs) with respect to other forms of carbon. Other catalysts (Co, Ni, and Fe/Co/Ni binary alloys) have been studied using the appropriate $MgAl_2O_4$-based solid solutions, with cobalt and equimolar Fe/Co alloys giving the best results.[12−15]

$Mg_{1−x}Co_xO$ powders were also studied as precursors and are notably interesting because a simple soaking in HCl allows one to separate the CNTs from the CNT−Co−MgO powders formed upon reduction in H_2/CH_4.[2,3] The so-obtained CNTs, 90% of which are SWNTs and double-walled CNTs (DWNTs) with a diameter between 0.7 and 3 nm, are dispersed individually rather than in bundles and have a very high specific surface area (ca. 950 m^2/g of carbon).[3] However, undesirable Co_3O_4 particles leading to thick carbon nanofibers rather than to CNTs may also form during the synthesis of the oxide using the combustion route.[16,17] It was shown[18] that a varying the urea/nitrate ratio allowed the formation of Co_3O_4 particles to be avoided, but more details on the valency and precise distribution of the cobalt ions in the MgO-based powders were not known. This prompted a study using $Mg_{1−x}Fe_xO$ oxides to take advantage of the powerful ^{57}Fe Mössbauer spectroscopy technique, although it was not expected to obtain a higher selectivity than when using cobalt because of the more numerous possibilities regarding the formation of iron phases compared to the formation of cobalt phases and also because of the easier formation of carbides.

In a companion paper,[19] we attempted to synthesize $Mg_{1−x}Fe_xO$ oxide solid solutions by the combustion route, with the aim of studying the influence of both the nitrate/urea ratio and the iron content on the valency and distribution of the iron ions and phases. Selected specimens are studied in the present paper. In

* To whom correspondence should be addressed. E-mail: laurent@chimie.ups-tlse.fr. Tel.: 00-33-(0)5-61-55-61-22. Fax: 00-33-(0)5-61-55-61-63.
† University of Ghent.
‡ Université Paul-Sabatier.

TABLE 1: Macroscopic Parameters of the CNTs−Fe−MgO Nanocomposite Powders[a]

composite powder	S_{ss} (m²/g)	S_n (m²/g)	S_o (m²/g)	C_n (wt %)	C_o (wt %)	ΔS (m²/g)	$\Delta S/\Delta C$ (m²/g)
Fe**5**U1R	16.5 ± 0.5	13.0 ± 0.4	7.4 ± 0.2	14.3 ± 0.3	0.0	5.6 ± 0.6	39 ± 6
Fe**5**U4R	6.4 ± 0.2	8.5 ± 0.3	7.4 ± 0.2	2.0 ± 0.1	0.5	1.1 ± 0.5	72 ± 35
Fe**5**U8R	45.6 ± 1.4	50.0 ± 1.5	33.2 ± 1.0	9.1 ± 0.2	0.3	16.8 ± 2.5	191 ± 36
Fe**10**U1R	26.2 ± 0.8	16.0 ± 0.5	8.0 ± 0.2	16.7 ± 0.3	0.0	8.0 ± 0.7	48 ± 6
Fe**10**U4R	6.6 ± 0.2	8.0 ± 0.2	5.7 ± 0.2	3.5 ± 0.1	0.1	2.3 ± 0.4	68 ± 15
Fe**10**U8R	51.8 ± 1.6	60.0 ± 1.8	37.0 ± 1.1	15.3 ± 0.3	0.3	23.0 ± 2.9	153 ± 26

[a] S_{ss}: specific surface area of the oxide precursor; S_n: specific surface area of the nanocomposite powder; S_o: specific surface area of the oxidized nanocomposite powder (5 min at 700 °C in air); C_n: carbon content in the nanocomposite powder; C_o: carbon content in the oxidized nanocomposite powder; $\Delta S = S_n - S_o$: CNT-quantity parameter; $\Delta S/\Delta C$: carbon-quality parameter ($\Delta C = C_n - C_o$).

the Fe/MgO oxides synthesized with the so-called stoichiometric urea/nitrate ratio (equal to unity), no Fe^{2+} ions are formed, and most of the Fe^{3+} ions form clusters and $MgFe_2O_4$-like particles that are poorly dispersed in this powder. The combustion conditions were therefore not sufficiently reducing. Increasing the ratio by a factor in the range of 3.5−4.5 leads to combustion conditions that could correspond to the stoichiometric region as defined by Zhang and Stangle.[20] Indeed, the so-obtained oxides contain about 40% of the total iron substituting as Fe^{2+} in the MgO lattice, and a large proportion of the Fe^{3+} ions are dispersed in the O_h sites of MgO. However, a local agglomeration of Fe^{3+} clusters can be expected in these samples. For a urea ratio increased by a factor of 8, the flame is greatly smothered during the combustion process, and the reaction temperature is markedly lower. Under these conditions, no Fe^{2+} ions are formed. The Fe^{3+} ions are involved in a bimodal size distribution of iron agglomerates: $MgFe_2O_4$-like particles larger than those detected for a urea ratio of 1 and very small Fe^{3+} clusters not detected for other urea ratios. It is noteworthy that these iron agglomerates are much better dispersed in the powders prepared using the urea ratio of 8 instead of 1.

The composite powders obtained upon reduction in a H_2/CH_4 gas atmosphere presented in this work have a fairly complex microstructure, with several iron species of various sizes dispersed inside and at the surface of the magnesia matrix and several carbon species including SWNTs and DWNTs. Characterizations are performed using ^{57}Fe Mössbauer spectroscopy and electron microscopy as well as a macroscopic method based on specific surface-area measurements.

Experimental Section

Synthesis of CNTs−Fe−MgO Nanocomposite Powders. The CNTs−Fe−MgO nanocomposite powders were obtained by selective reduction in a H_2/CH_4 atmosphere of the oxide powders prepared by combustion.[20] Typically, 1 g of oxide powder was spread in an alumina vessel so that the powder layer did not exceed 5 mm in thickness. The reaction was carried out at atmospheric pressure in a fixed-bed flow reactor (Adamel CT5HT tubular furnace with a silica reactor). The proportion of CH_4 was 18 mol %, giving rise to supersaturation in the H_2/CH_4 atmosphere[21] at temperatures required for the formation of the CNTs (above 700 °C). The gas flow was fixed at 15 L/h, and the gas mixture was dried on P_2O_5. The thermal cycle was the following: a heating rate of 5 °C/min up to 1000 °C, no dwell at 1000 °C, and a cooling rate of 5 °C/min to room temperature (RT).

For the sake of brevity, the samples will be referred to according to the following example: Fe10U4 will be used for a supposed $Mg_{0.90}Fe_{0.10}O$ solid solution prepared with a urea ratio of 4, and the corresponding nanocomposite powder will
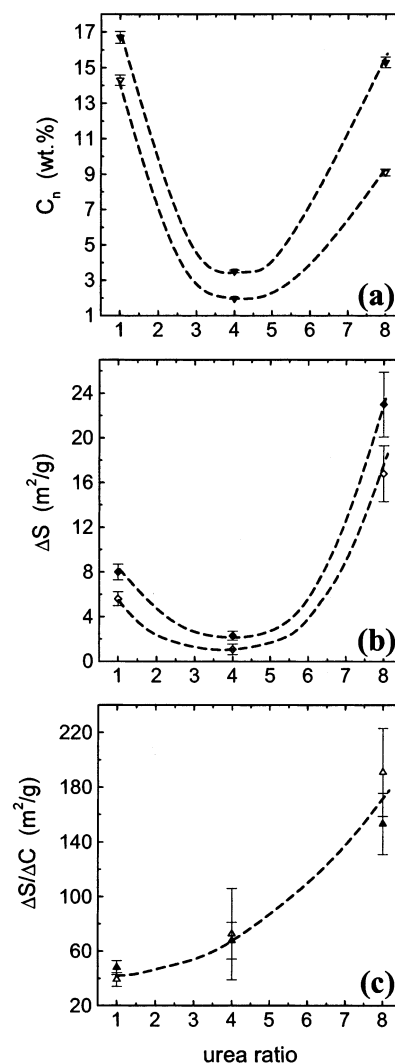

Figure 1. Carbon content C_n (a), CNT-quantity parameter ΔS (b), and carbon-quality parameter $\Delta S/\Delta C$ (c) for the CNTs−Fe−MgO nanocomposite powders versus the urea ratio used for the combustion of the corresponding oxide precursors. The open symbols correspond to Fe5R nanocomposite powders, and the solid symbols correspond to Fe10R nanocomposite powders. The dashed lines are guides for the eye.

be designated as Fe10U4R. Fe5 and Fe5R powders contain 2 times less iron.

Characterization. A method based on carbon element analysis and specific surface-area measurements[8,22] was used to characterize the composite powders on the macroscopic scale to produce quantitative data that are useful in comparing the different specimens. Parts of the CNTs−Fe−MgO powders were oxidized in air to eliminate the carbon, as required for the study. The specific surface areas of the powders obtained after
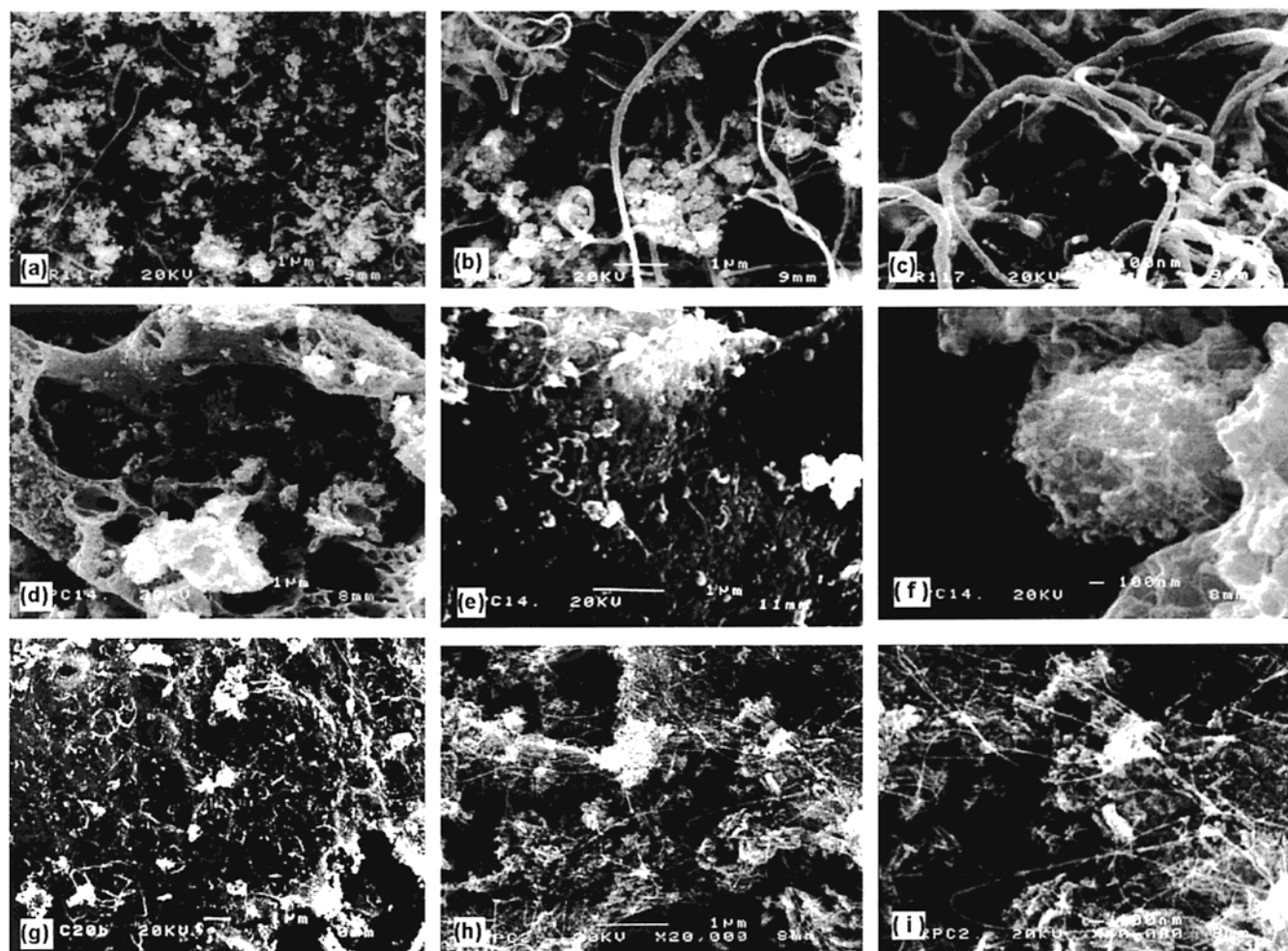
Carbon Nanotubes by a CVD Method

J. Phys. Chem. B, Vol. 106, No. 51, 2002 **13201**

Figure 2. SEM images of Fe10U1R (a, b, c), Fe10U4R (d, e, f), and Fe10U8R (g, h, i) at different magnifications.

reduction (S_n) and of the oxidized specimens (S_o) were measured by the BET method using N_2 adsorption at liquid N_2 temperature in a Micromeritics FlowSorb II 2300 apparatus. This instrument gives a specific surface-area value from one point (i.e., one adsorbate pressure) and requires calibration. The reproducibility of the results was determined to be in the ±3% range. $\Delta S = S_n - S_o$ represents the quantity of CNTs.[8,10,22] The oxidation process was limited to 5 min at 700 °C to avoid the sintering of the matrix grains and the coalescence of the particles, which could give rise to undervalued S_o values and thus overvalued ΔS values. The carbon content of the powders obtained after reduction (C_n) was determined by flash combustion with an accuracy of ±2%. Carbon traces on the order of 0.3 wt % were also detected in the specimens oxidized at 700 °C (C_o). $\Delta S/\Delta C$ with $\Delta C = C_n - C_o$ is considered to represent the quality of the deposited carbon, a higher-quality parameter principally corresponding to more carbon in tubular form and/or CNTs with fewer walls and/or fewer bundled CNTs.[8,22] X-ray diffraction (XRD) patterns were recorded with a Siemens D501 diffractometer using Cu Kα radiation and were computer analyzed with the GUFI 5.0 program.[23] For lattice-parameter measurements, the powders were mixed with NaCl as an internal standard, and the calculations were performed with the UnitCell program.[24] The crystallite sizes were evaluated from the widths at half-maximum of the diffraction peaks using the well-known Scherrer formula, with an accuracy on the order of 20%.

Mössbauer spectra (MS) were recorded with a ^{57}Co (Rh) source using a conventional time-mode spectrometer with a constant-acceleration drive and a triangular reference signal. The accumulation of the data was performed in 1024 channels until a background of at least 10^6 counts per channel was reached. The spectrometer was calibrated by collecting at RT the MS of a standard α-Fe foil, and the isomer-shift values quoted hereafter are with reference to this standard. The measured absorbers were prepared with the amount of powder corresponding to 10 mg of iron atoms per square centimeter. Measurements were performed at RT and at 80 K in a cryostat cooled with liquid nitrogen. The spectra were generally analyzed assuming symmetrical components with Lorentzian line shapes. Asymmetrical Mössbauer patterns were fitted with a model-independent hyperfine-field or quadrupole-splitting distribution with Lorentzian-shaped elemental spectra, where linear correlations between the isomer shift and/or quadrupole shift and the hyperfine field of a distributed sextet and between the isomer shift and the quadrupole splitting of a distributed doublet can be used.[25]

The CNTs−Fe−MgO nanocomposite powders were observed with a JEOL JSM 6400 scanning electron microscope (SEM) and with a JEOL 2010 transmission electron microscope (TEM). The latter microscope allows us to obtain high-resolution images, where the fringes corresponding to the walls of isolated CNTs are clearly resolved. Moreover, by using a short image-capture time, many images are obtained at different places in a sample in a short time. It is then possible to obtain significant statistical results on the distribution of the CNTs' number of walls and diameters in a powder. At least 70 individual CNTs per sample were considered in these distributions.
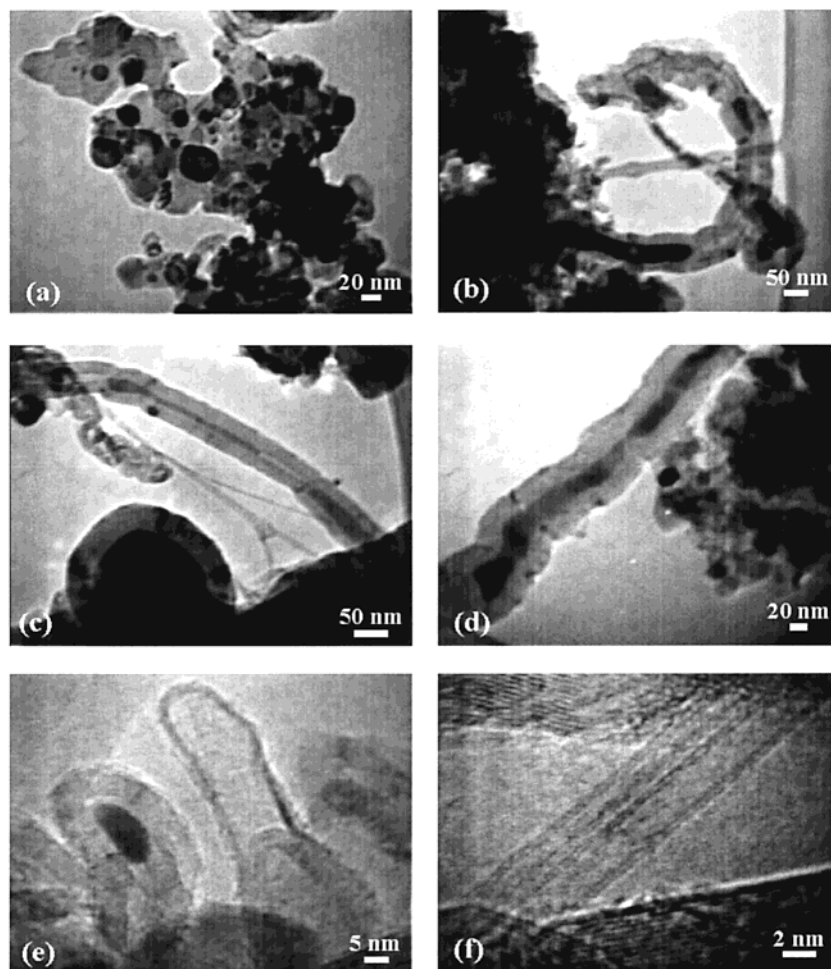
Figure 3. TEM images of Fe10U1R.

Results and Discussion

Carbon Content and Specific Surface Areas. Table 1 gives the macroscopic parameters (C_n, ΔS, and $\Delta S/\Delta C$) of the CNTs−Fe−MgO nanocomposite powders together with the specific surface-area (S_{ss}) of the corresponding oxide precursors.[20] The macroscopic parameters are plotted versus the urea ratio used for the combustion of the corresponding oxide precursors in Figure 1.

Powders Fe10R will be discussed first. C_n is very high for Fe10U1R, decreases steeply for Fe10U4R, and increases for Fe10U8R to reach a value only slightly lower than that of Fe10U1R (Figure 1a). ΔS decreases from Fe10U1R to Fe10U4R and subsequently increases to reach a maximum value for Fe10U8R (Figure 1b). $\Delta S/\Delta C$ increases from Fe10U1R to Fe10U4R and reaches a maximum value for Fe10U8R (Figure 1c). The high carbon content in Fe10U1R is associated with a rather small CNT quantity, leading to very poor quality of the carbon in this powder. Moreover, S_n for Fe10U1R is smaller than S_{ss} (Table 1), showing that the extra surface area due to the expected tubular carbon is smaller than the diminution of the surface area due to the sintering of the matrix grains. In Fe10U4R, the low carbon content results in a low CNT quantity. However, other carbon species must also be present, leading to rather low carbon quality. For Fe10U8R, the high carbon content corresponds to a high CNT quantity, resulting in higher carbon quality.

C_n and ΔS for the Fe5R composite powders (Table 1) show the same evolution as for the Fe10R composite powders, but

the values are slightly lower. This reflects the smaller amount of iron in the materials. However, the $\Delta S/\Delta C$ values are similar (Table 1).

Scanning Electron Microscopy. SEM images of Fe10U1R, Fe10U4R, and Fe10U8R are shown in Figure 2. Fe10U1R (Figure 2a−c) shows compact grains consisting of small primary grains. Numerous thick, short carbon nanofibers are observed. On the higher-magnification images (Figure 2b and c), one can detect a small proportion of thin carbon filaments resembling bundles of CNTs.[2,3,8−11,13−15] Fe10U4R (Figure 2d−f) appears to be a porous foam with large open cavities. Much less deposited carbon is observed, in agreement with the very low C_n value, but thin filaments can nevertheless be observed at a higher magnification (Figure 2f). Fe10U8R (Figure 2g−i) is more porous, and the primary grains are small and loosely packed. Most carbon filaments are thin and appear to be typical CNTs bundles. A comparison of the high-magnification images of Fe10U1R and Fe10U8R (Figure 2f and i) could indicate that a large proportion of CNTs, particularly individual CNTs, are still unobservable for Fe10U8R since the material contains a similar amount of carbon. These results are in agreement with the above macroscopic study. The MgO matrix microstructure in the nanocomposite powders is rather similar to that observed for the corresponding oxide precursors.[20]

Transmission Electron Microscopy. Typical TEM images of Fe10U1R, Fe10U4R, and Fe10U8R are presented in Figures 3, 4, and 5, respectively. For Fe10U1R, Figure 3a shows metal nanoparticles (dark spots) at the surface of the oxide matrix. These particles are too large to have been involved in the
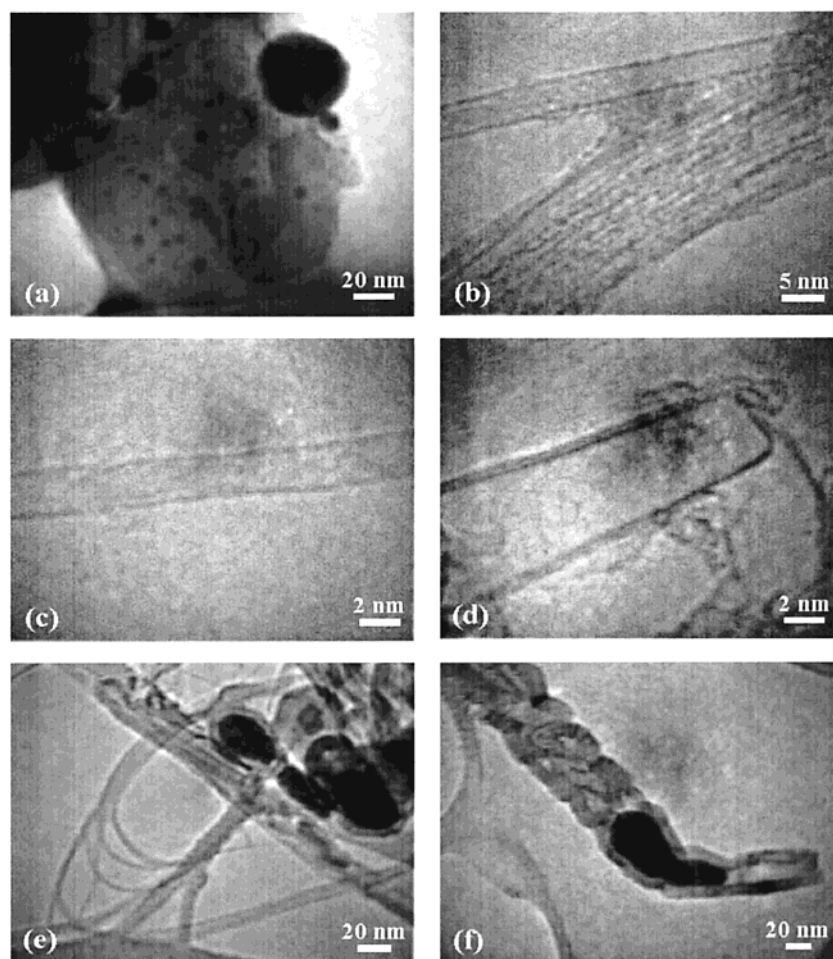
Carbon Nanotubes by a CVD Method

J. Phys. Chem. B, Vol. 106, No. 51, 2002 **13203**

Figure 4. TEM images of Fe10U4R.

formation of CNTs. More details about the thick carbon nanofibers are revealed in Figure 3b−e. They are irregularly shaped and curved, and the inner cavity is partially filled with elongated Fe and/or Fe_3C particles. The inner and outer diameters are about 10 and 80 nm, respectively. The observation of such short, thick nanofibers in a powder is a typical indication that the iron ions are not well dispersed in the starting material[10,11] and that relatively large particles are able to form and catalyze the nanofibers' growth. In Figure 3c, note the particle with a very large diameter (>100 nm) covered by numerous graphene sheets. Figure 3f shows two DWNTs, this form of carbon being difficult to find among the thick nanofibers present everywhere in the sample. These observations are in agreement with the low CNT-quality parameter $\Delta S/\Delta C$ (Table 1) since the specific surface area of nanofibers is much lower than that of CNTs.[22]

Figure 4a reveals metal nanoparticles (dark spots) in Fe10U4R. Many small particles (diameter <10 nm) are observed, but very large particles are also present. Figure 4b shows a bundle of CNTs at a point where one CNTs is leaving (or joining) the bundle. Some disordered carbon is present at the junction. Parts c and d of Figure 4 show a SWNT and a DWNT, respectively. The latter seems to be partially covered by disordered carbon. In Figure 4e, large particles covered by graphene sheets are observed. As a consequence of the presence of large particles, thick carbon nanofibers have been formed (Figure 4f), but they are less abundant than in Fe10U1R, as revealed by the SEM images.

For Fe10U8R, Figure 5a shows a bundle of CNTs coming out of the matrix. The dark spots are metal particles. Figure 5b reveals the presence of nanofibers, but they are thinner than in previous samples and appear to be a minor component compared to the proportion of CNTs. Figure 5c−f shows CNTs with one, two, or three walls. As already observed for Fe10U4R, disordered carbon appears at some places on the surface of the CNTs (Figure 5e and f). Figure 5e shows a SWNT with an angle of $a = 120°$. Such angled CNTs were frequently observed for this powder.

Figure 6 presents histograms of the particle-size distributions in Fe10U1R, Fe10U4R, and Fe10U8R obtained by measuring more than 100 particles on TEM images. The particles in Fe10U1R have a wide size range from a few nanometers to 100 nm, with an average diameter of 32.1 nm. In Fe10U4R and Fe10U8R, the proportion of small particles is much higher, and the average particle diameters are 8.3 and 8.9 nm, respectively. Moreover, almost 60% of the particles in Fe10U4R are smaller than 5 nm, whereas in Fe10U8R, the maximum proportion appears to be between 5 and 10 nm. However, Fe10U4R also contains some large particles that are not observed in Fe10U8R. The proportion of small particles (diameter <5 nm) measured on the TEM images is probably undervalued because of the difficulty in detecting them compared to detecting large particles. However, all images were analyzed in the same way so that the histograms can uncover different tendencies for the different samples. Moreover, most of the measured particles are not associated with CNTs, but they can nevertheless be considered to be representative of the general trend of the particle-size distribution in the sample.

Figure 7 compares the particle-size distributions and the nanofiber outer-diameter distributions in Fe10U1R. These
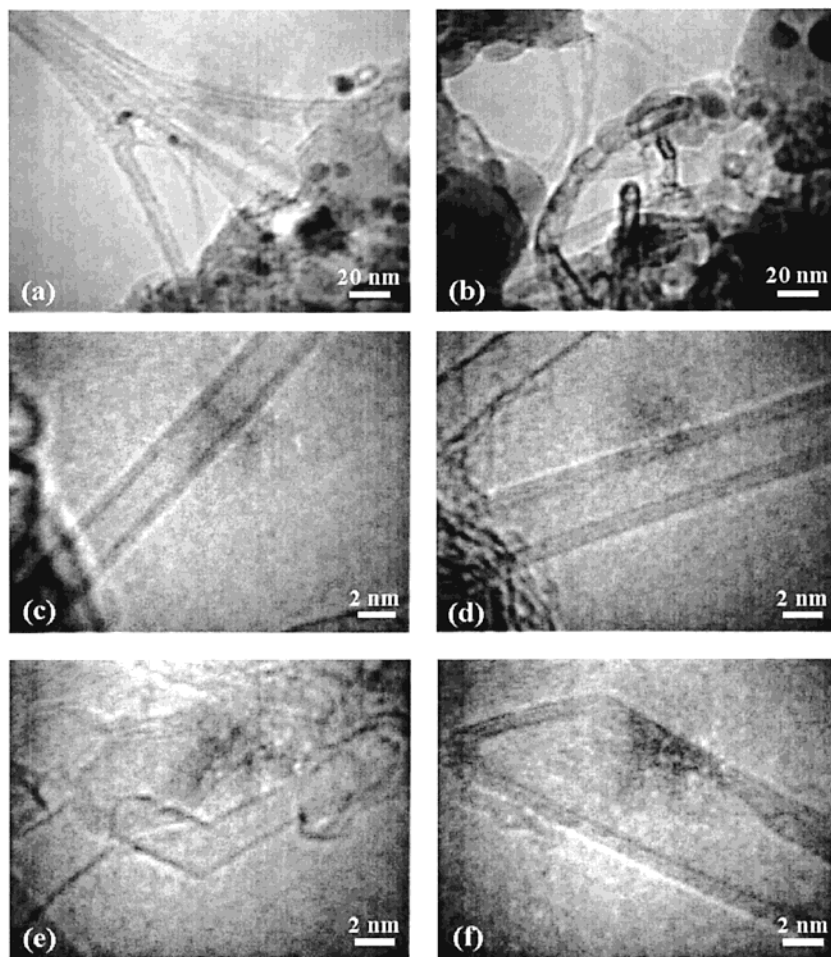
Figure 5. TEM images of Fe10U8R.

distributions and the corresponding average diameters (32.1 and 32.7 nm, respectively) are similar, implying a narrow association between the large particles and the nanofibers.

Figure 8 compares the number of walls of CNTs, the SWNT diameter, and the DWNT inner-diameter distributions in Fe10U4R and Fe10U8R. The distributions of the numbers of walls show that most CNTs are SWNTs or DWNTs. Indeed, for Fe10U4R, the sum of the proportions of SWNTs and DWNTs is 95%, DWNTs being slightly in the majority (Figure 8a). This number decreases to 80% for Fe10U8R, which contains fewer DWNTs and more SWNTs and 3WNTs (Figure 8b). Note that the average number of walls, which is only a statistical parameter since it is not an integer, is the same for the two samples (N_m = 1.7). The width of the diameter distributions for the SWNTs in Fe10U4R and Fe10U8R (Figure 8c and d) is similar to that (1−5 nm) reported for SWNTs prepared by catalytic methods.[2−4,11,26−33] As pointed out by Dai et al.,[26] the distribution in the tube diameter reflects a mechanism in which the diameter is established by the catalytic particle. In contrast, the inner-diameter distributions of the DWNTs are broader. It is also noteworthy that for DWNTs in Fe10U4R, as opposed to SWNTs, a large proportion (45%) of the inner diameters are within the smallest diameter class. The average inner diameter of the DWNTs in Fe10U4R is also smaller than the average diameter of the SWNTs (1.8 and 2.2 nm, respectively). Similar observations were made in a previous work[4] for the DWNTs and SWNTs synthesized by reduction in H_2/CH_4 of an $Al_{1.8}$-$Fe_{0.2}O_3$ oxide powder. Two explanations can be proposed. First, this could reflect for part of the DWNTs the internal growth of the second wall, possibly by the yarmulke mechanism.[26] A

characteristic of this mechanism indeed is that the outermost layer grows first. A second carbon cap (yarmulke) can form underneath the first, spaced by roughly the interlayer spacing of graphite and forcing it to lift up by forming a tube whose open end remains chemisorbed to the catalytic particle. Second, another phenomenon to take into account is that the smaller catalytic particles (<2 nm) are more active than the larger ones because of a higher surface curvature. They produce more carbon at a higher rate and therefore could tend to form DWNTs rather than SWNTs. For Fe10U8R, however, this trend is less marked, and the average inner diameters of the DWNTs equivalent to the average diameter of the SWNTs are 2.1 and 2.0 nm.

X-ray Diffraction. The XRD patterns of Fe10U1R, Fe10U4R, and Fe10U8R are reproduced in Figure 9. The five characteristic peaks of MgO are recognized. The MgO unit-cell parameters a and the average MgO crystallite sizes $\varnothing$ are reported in Table 2, together with the values for the corresponding oxide precursors.[20] The MgO unit-cell parameter of the composite powders is maximum for Fe10U4R, with similar lower values for Fe10U1R and Fe10U8R, revealing the same trend as in the oxide powders. However, the MgO unit-cell parameters tend to be higher for the composite powders than for the parent oxide powders, suggesting a possibly larger proportion of substituting Fe^{2+} ions in the MgO lattice of the composite powders. The average MgO crystallite size has a maximum value for Fe10U4R, a minimum value for Fe10U8R, and an intermediate value for Fe10U1R. This trend is in agreement with the observations made on the SEM images of the previous section and is similar to the trend in the oxide powders. However, the
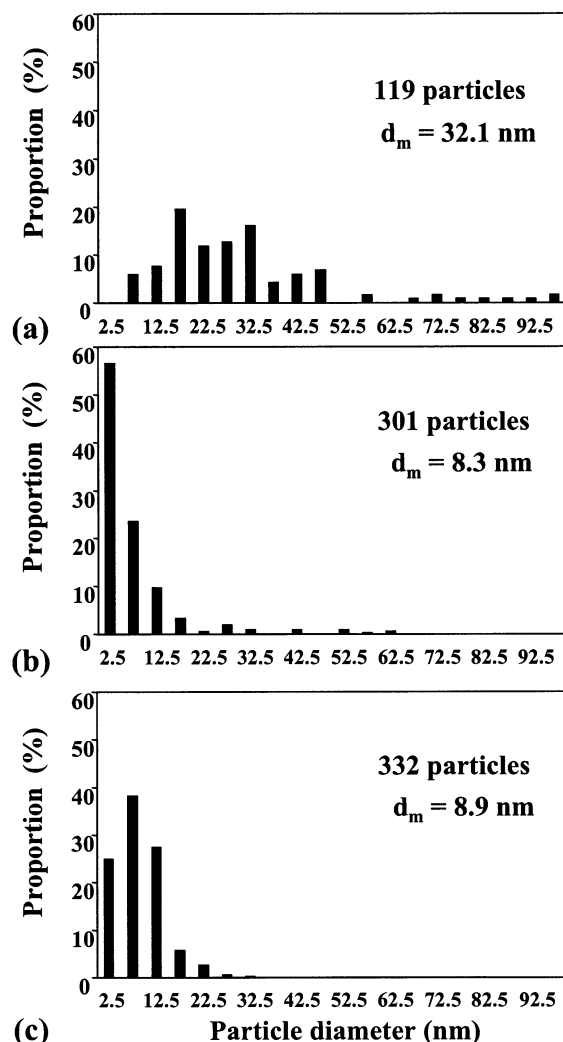
Figure 6. Particle-size distributions in Fe10U1R (a), Fe10U4R (b), and Fe10U8R (c) evaluated from TEM images (similar to those shown in Figures 3−5, respectively). Each class noted by a value of *x* nm corresponds to particle sizes contained between (*x* − 2.5 nm) and (*x* + 2.5 nm). For all distributions, the number of measurements and the average particle size (*d*$_m$) are indicated.
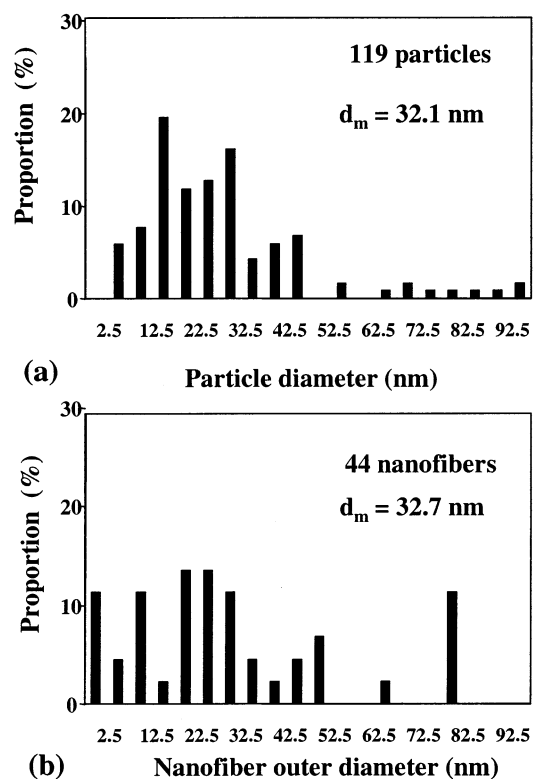

Figure 7. Particle-size (a) and nanonanofiber outer-diameter (b) distributions in Fe10U1R evaluated from TEM images (similar to those shown in Figure 3). Each class noted by a value of *x* nm corresponds to particle sizes or nanofiber outer diameters contained between (*x* − 2.5 nm) and (*x* + 2.5 nm). For both distributions, the number of measurements and the average value (*d*$_m$ and *do*$_m$) are indicated.

average crystallite sizes seem to be slightly higher in the composite powders than in the parent oxide powders. This is due to a little sintering of the matrix grains during the reduction process at high temperature.

Besides the MgO peaks, small peaks characteristic of α-Fe and Fe$_3$C and a peak characteristic of the distance between two graphene sheets in MWNTs and/or in graphite are observed in the XRD patterns of Fe10U1R, Fe10U4R, and Fe10U8R (Figure 9). Their intensity is minimum for Fe10U4R. No γ-Fe is detected.

^{57}Fe Mössbauer Spectroscopy. Figure 10 shows the MS of the Fe5R and Fe10R nanocomposite powders measured at RT. The corresponding Mössbauer parameters are given in Table 3. Figure 11 shows the MS of the Fe10R nanocomposite powders measured at 80 K. The corresponding Mössbauer parameters are given in Table 4.

Paramagnetic Fe^{2+} is detected in all MS, and an extra Fe^{3+} doublet was used to fit the MS of the FeU1R and FeU8R nanocomposite powders. Moreover, the three characteristic phases of similarly synthesized CNTs−Fe−Al$_2$O$_3$[4] and CNTs−Fe−MgAl$_2$O$_4$[14] nanocomposite powders are observed in all MS (i.e., a sextet of ferromagnetic α-Fe, a sextet of ferromagnetic Fe$_3$C, and a singlet of paramagnetic γ-Fe−C). At 80 K, the

same iron phases are resolved with nearly identical proportions, and no indication of the presence of other phases was found.

For Fe5U4R and Fe10U4R, the Fe^{2+} proportion is very high (∼70%). A quadrupole-splitting distribution was used to fit this component, both at RT and at 80 K (Figures 10c and d and 11c). Two maxima are evaluated in the distributions at RT (Figure 10c and d). At 80 K, the two maxima are more separated, the second one showing a highly increased quadrupole-splitting value as compared to that at RT (Figure 11d). Referring to our results[20] and to those reported by several authors,[34−40] these two maxima are attributed to Fe^{2+} ions distributed in the octahedral (O_h) sites of MgO, the second maximum revealing Fe^{2+} clusters. The proportions of Fe^{2+} ions in Fe5U4R and Fe10U4R are equivalent (Table 3), implying that the number of Fe^{2+} ions is twice as large in Fe10U4R as in Fe5U4R. Moreover, the second maximum in the Fe^{2+} quadrupole-splitting distributions in Fe10U4R is higher than the first (Figures 10d and 11d), contrary to the maxima in the Fe^{2+} quadrupole-splitting distribution in Fe5U4R (Figure 10c), revealing a higher proportion of Fe^{2+} ions that form clusters in Fe10U4R than in Fe5U4R. The FeU1R and FeU8R nanocomposite powders contain many fewer Fe^{2+} ions than the FeU4R nanocomposite powders and a single Fe^{2+} doublet allowed to obtain a proper fit of the MS at RT and at 80 K (Figures 10a, b, e, and f and 11a and e). The Fe^{2+} proportions in Fe5U1R and Fe10U1R are similar, and the Fe^{2+} proportion in Fe5U8R is slightly lower than in Fe10U8R (Table 3). This implies again at least twice as many Fe^{2+} ions in the Fe10R nanocomposite powders as in the Fe5R powders. Moreover, the quadrupole splittings of the Fe^{2+} doublets in Fe10U1R and Fe10U8R are larger than those in Fe5U1R and Fe5U8R (Table 3). This suggests again that a larger number of Fe^{2+} ions in the MgO
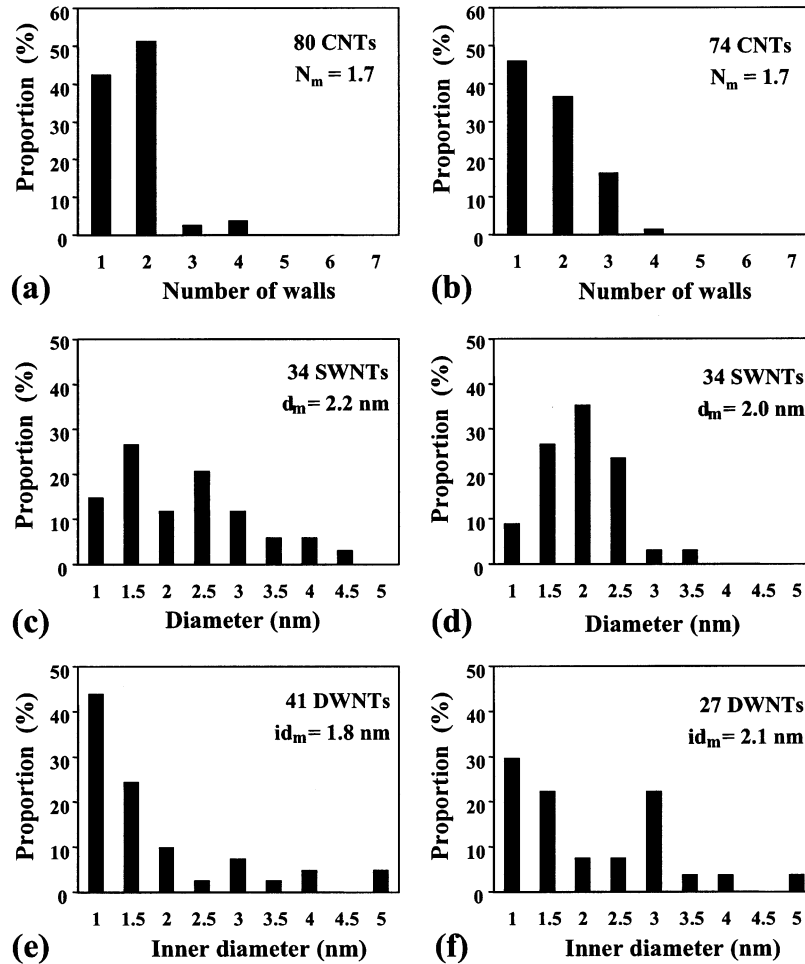
Figure 8. Number-of-walls (a, b), SWNT diameter (c, d) and DWNT inner-diameter (e, f) distributions in Fe10U4R and Fe10U8R, respectively, evaluated from TEM images (similar to those shown in Figures 4 and 5, respectively). Each class noted by a value of x nm corresponds to CNT (inner-)diameters contained between ($x − 0.25$ nm) and ($x + 0.25$ nm). For all distributions, the number of measurements and the average value (N_m, d_m, or id_m) are indicated.
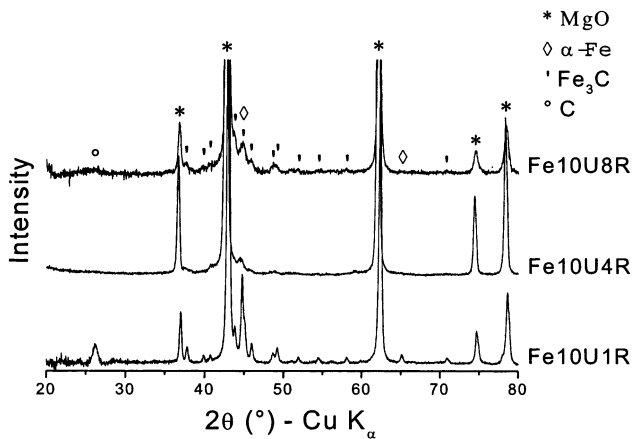

Figure 9. XRD patterns of Fe10U1R, Fe10U4R, and Fe10U8R.

TABLE 2: MgO Unit-Cell Parameter a and Average MgO Crystallite Size $\varnothing$ of Fe10U1R, Fe10U4R, and Fe10U8R and of the Corresponding Oxide Precursors

composite powder	a (oxide) (nm)	a (composite) (nm)	$\varnothing$ (oxide) (nm)	$\varnothing$ (composite) (nm)
Fe**10U1R**	0.4213 ± 0.0001	0.4216 ± 0.0002	33.6 ± 6.7	44.1 ± 8.8
Fe**10U4R**	0.4221 ± 0.0004	0.4226 ± 0.0004	52.2 ± 10.4	58.3 ± 11.7
Fe**10U8R**	0.4212 ± 0.0004	0.4217 ± 0.0003	24.2 ± 4.8	26.1 ± 5.2

in a matrix can exhibit bulk Mössbauer parameters down to a diameter of 2 nm. In particular, Boudart et al.[34] have not found any deviation from bulk parameters for α-Fe nanoparticles of an average diameter of 2.5 nm produced on a MgO support. These particles can be compared to the α-Fe nanoparticles detected in CNTs−Fe−Al$_2$O$_3$[4] and CNTs−Fe−MgAl$_2$O$_4$[14] nanocomposite powders.

Fe$_3$C has two inequivalent crystallographic Fe sites[43] that are magnetically and electronically very similar. In previous works,[4,14] the Fe$_3$C ferromagnetic phase was satisfactorily fitted with a single sextet. The Fe$_3$C proportions in the FeU1R and FeU8R nanocomposite powders are large ($\sim$50%). For these samples, an asymmetry in the Fe$_3$C six-line patterns is obvious, notably in the MS measured at 80 K: in particular, the first line is deeper and narrower than the sixth line (Figure 11a and e). This is in agreement with Bi et al.,[44] who have shown that the differences between the Mössbauer parameters of the two Fe sites of Fe$_3$C increase with decreasing temperature. A better

lattice favors the formation of Fe^{2+} clusters. In all Fe10R nanocomposite powders, the (super)paramagnetic Fe^{2+} proportions are equivalent at RT and at 80 K (Tables 3 and 4), and the MS at 80 K (Figure 11) show no magnetic splitting resulting from the Fe^{2+} clusters.

The Mössbauer parameters of α-Fe are those of bulk iron, and no superparamagnetic relaxation is observed. Hence, size effects are not reflected in the Mössbauer parameters. However, small particles can be expected. Indeed, different works[41,42] have shown that α-Fe particles dispersed on a support or embedded

Carbon Nanotubes by a CVD Method

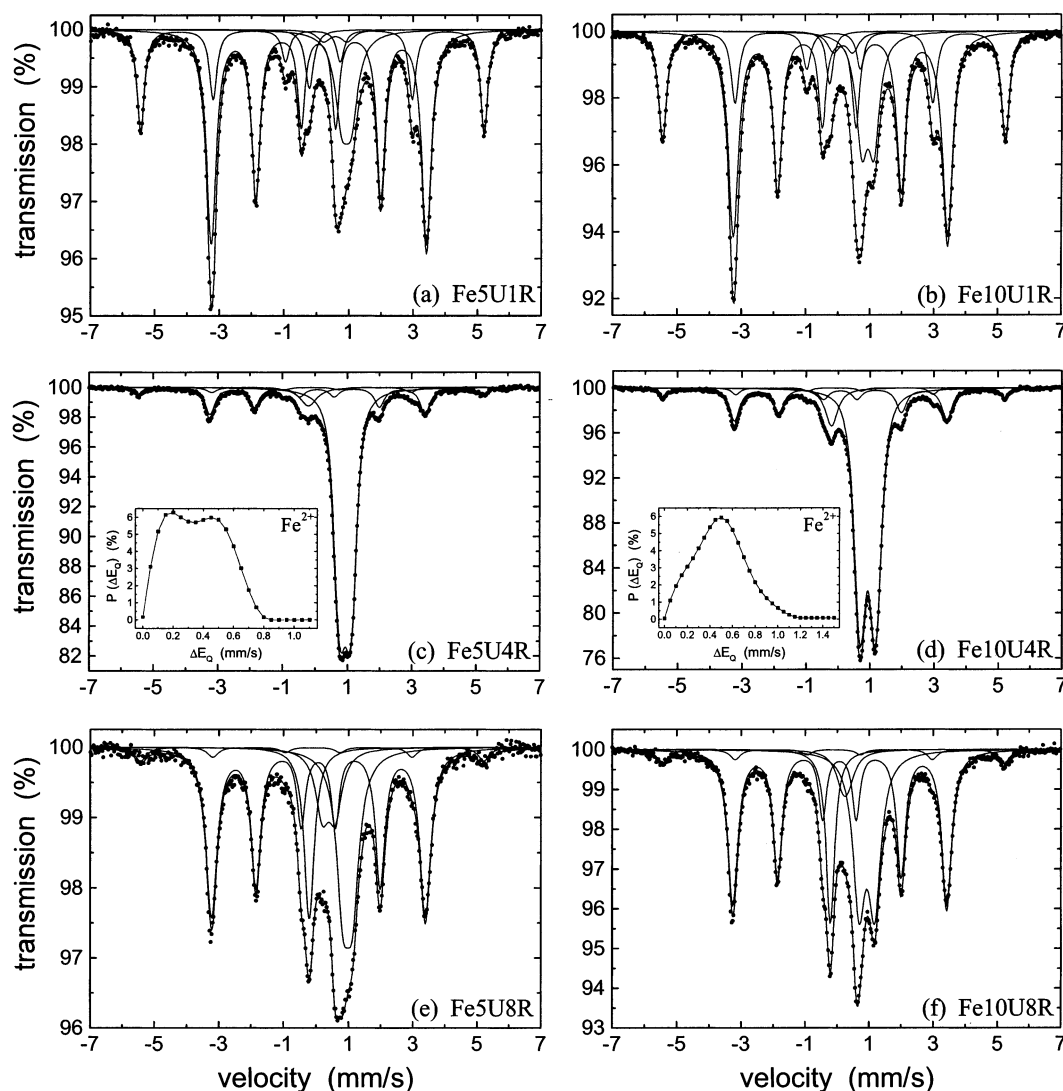*J. Phys. Chem. B, Vol. 106, No. 51, 2002* **13207**

Figure 10. MS of the CNTs−Fe−MgO nanocomposite powders measured at RT: Fe5U1R (a), Fe10U1R (b), Fe5U4R with the Fe^{2+} quadrupole-splitting distribution (c), Fe10U4R with the Fe^{2+} quadrupole-splitting distribution (d), Fe5U8R (e), and Fe10U8R (f).

TABLE 3: Mössbauer Parameters of the CNTs−Fe−MgO Nanocomposite Powders Measured at RT^a

composite powder	para Fe^{2+}				para Fe^{3+}				ferro α-Fe					ferro Fe_3C					para γ-Fe−C		
	δ	ΔE_Q	Γ	P	δ	ΔE_Q	Γ	P	δ	H_{hf}	$2\epsilon_Q$	Γ	P	δ	H_{hf}	$2\epsilon_Q$	Γ	P	δ	Γ	P
Fe**5U1R**	1.04	0.29	0.50	14.5	0.69	0.73	0.49	2.0	0.00	330	0^b	0.29	21.5	0.18	207	0.02	0.27	58.5	−0.11	0.31	3.5
Fe**5U4R**	1.04	0.19^c	0.28	71.5					0^b	330^b	0^b	0.38	5.5	0.19	206	0.02	0.36	18.0	−0.10	0.62	5.0
		0.45^c																			
Fe**5U8R**	1.09	0.29	0.49	23.5	0.50	0.40	0.50	11.0	0^b	330^b	0^b	0.36	4.0	0.18	205	0.02	0.30	50.0	−0.10	0.37	11.5
Fe**10U1R**	1.07	0.38	0.43	16.0	0.29	0.61	0.47	3.0	0.00	331	0^b	0.29	23.5	0.18	207	0.02	0.28	55.0	−0.13	0.27	2.5
Fe**10U4R**	1.04	0.20^d	0.27	68.5					0^b	330^b	0^b	0.31	5.0	0.18	206	0.02	0.38	19.5	−0.10	0.48	7.0
		0.50^d																			
Fe**10U8R**	1.04	0.49	0.46	28.5	0.36	0.16	0.53	5.5	0^b	330^b	0^b	0.35	5.0	0.18	207	0.01	0.29	49.5	−0.11	0.32	11.5

^{a} Para: paramagnetic; ferro: ferromagnetic; H_{hf}: hyperfine field (kOe); δ: (average) isomer shift (mm/s); ΔE_Q: quadrupole splitting (at the maxima of the distribution) (mm/s); $2\epsilon_Q$: quadrupole shift (mm/s); Γ: Lorentzian line width (mm/s); P: proportion (%). ^{b} Fixed parameter. ^{c} Quadrupole-splitting distribution from 0.00 to 1.10 mm/s. ^{d} Quadrupole-splitting distribution from 0.00 to 1.50 mm/s.

fit of the present Fe_3C patterns at 80 K was obtained with a hyperfine-field distribution including linear correlations between the isomer shift and hyperfine field and between the quadrupole shift and hyperfine field. Two maxima clearly appear in the distributions (Figure 11b and f) with Mössbauer parameters comparable to those obtained by Bi et al.[44] for the two Fe sites of Fe_3C measured at 12 K. However, the proportion of the Fe_3C phase obtained from this fitting procedure is similar to the one obtained using a single sextet. The fitting procedure, therefore, does not have a significant influence on the present discussion.

Moreover, Bi et al.[44] measured the MS of Fe_3C particles as small as 5 nm and could not detect any significant differences in the Mössbauer parameters of the two components compared to that of bulk Fe_3C. In particular, no superparamagnetic relaxation takes place, even at RT. The more accurate fit of the Fe_3C phase proposed here confirms that the Mössbauer study does not provide information about the size of the Fe_3C particles but does not exclude sizes on the order of the CNTs' diameters.

Figure 12 shows the RT proportions of the iron phases in the Fe5R and Fe10R nanocomposite powders versus the urea
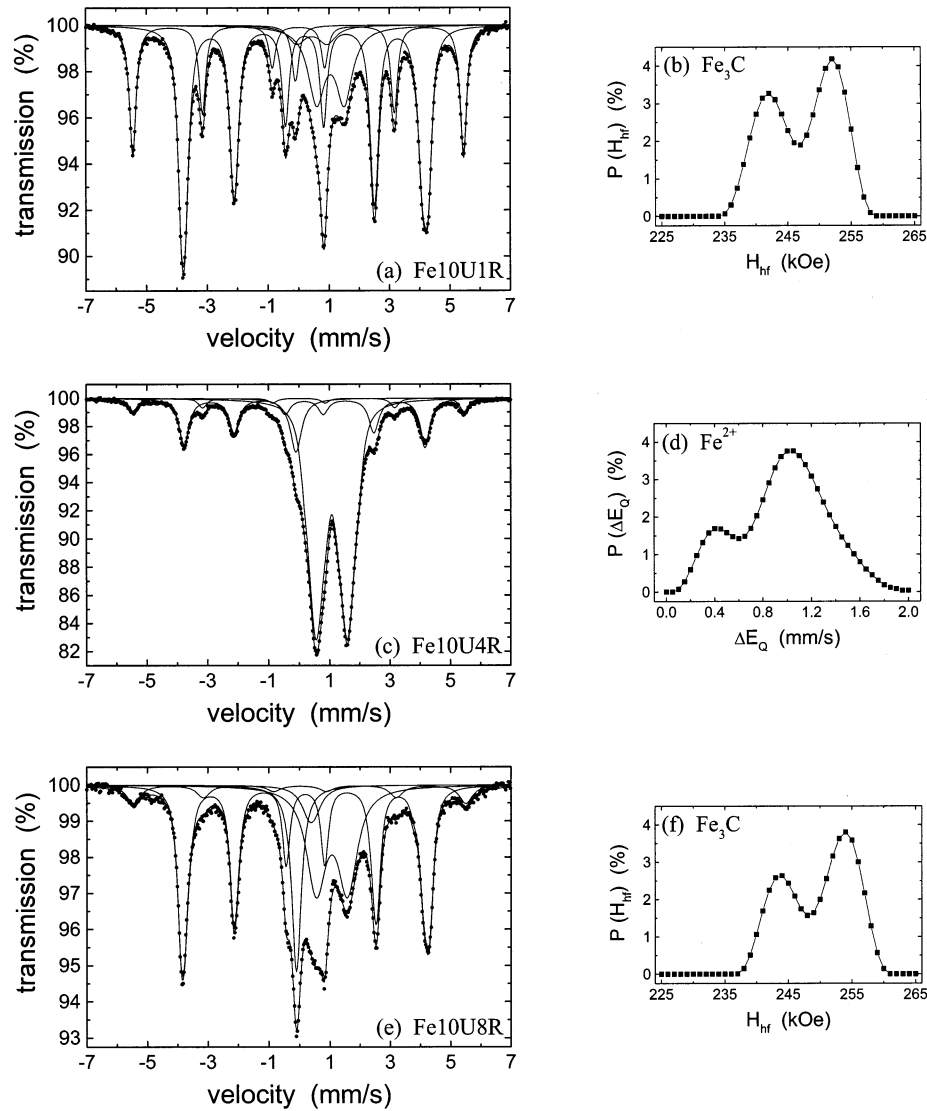
Figure 11. MS of the CNTs−Fe−MgO nanocomposite powders measured at 80 K: Fe10U1R (a) and the corresponding Fe$_3$C hyperfine-field distribution (b), Fe10U4R (c) and the corresponding Fe^{2+} quadrupole-splitting distribution (d), and Fe10U8R (e) and the corresponding Fe$_3$C hyperfine-field distribution (f).

TABLE 4: Mössbauer Parameters of the Fe10R Nanocomposite Powders Measured at 80 K^a

composite powder	para Fe^{2+}				para Fe^{3+}				ferro α-Fe					ferro Fe$_3$C					para γ-Fe−C		
	δ	ΔE_Q	Γ	P	δ	ΔE_Q	Γ	P	δ	H_{hf}	$2\epsilon_Q$	Γ	P	δ	H_{hf}	$2\epsilon_Q$	Γ	P	δ	Γ	P
Fe10U1R	1.16	0.92	0.66	16.0	0.55	1.00	0.70	4.0	0.11	338	0^b	0.26	22.5	0.30	242^d	−0.02	0.27	55.0	0.00	0.28	2.5
														0.31	252^d	0.02					
Fe10U4R	1.18	0.40^c	0.33	68.5					0.11	339	0^b	0.32	5.0	0.29	246	0.02	0.39	20.0	0.01	0.45	6.5
		1.03^c																			
Fe10U8R	1.18	1.02	0.72	27.0	0.50	0.17	0.62	4.5	0.13	340	0^b	0.52	7.0	0.29	244^d	−0.02	0.29	49.0	0.01	0.38	12.5
														0.31	254^d	0.01					

^{a} Para: paramagnetic; ferro: ferromagnetic; H_{hf}: hyperfine field (at the maxima of the distribution) (kOe); δ: (average) isomer shift (mm/s); ΔE_Q: quadrupole splitting (at the maxima of the distribution) (mm/s); $2\epsilon_Q$: quadrupole shift (mm/s); Γ: Lorentzian line width (mm/s); P: proportion (%). ^{b} Fixed parameter. ^{c} Quadrupole-splitting distribution from 0.00 to 2.00 mm/s. ^{d} Hyperfine-field distribution from 225 to 265 kOe.

ratio used for the combustion of the corresponding oxide precursors[20] (results from Table 3). For each urea ratio, all proportions are similar for the Fe5R and Fe10R nanocomposite powders so that only the latter ones will be considered in the following discussion. Moreover, the amount of iron in the samples being constant, the evolution of the proportions can be assimilated with the evolution of the amounts of the different iron phases in the oxide and composite powders. From the previous results,[4,14] the iron phases detected in the present CNTs−Fe−MgO nanocomposite powders can be correlated to the nature and the structure of the corresponding oxide precur-

sors, allowing us to understand the nature and quantity of the carbon species presented above. The amount of Fe^{2+} in all CNTs−Fe−MgO nanocomposite powders (Table 3) is larger than that in the corresponding oxide precursors. This amount of Fe^{2+} is minimal for Fe10U1R, increases sharply to reach a maximum for Fe10U4R, and decreases for Fe10U8R, which exhibits a higher value than Fe10U1R (Figure 12b). The increase in the amount of Fe^{2+} upon reduction of the Fe/MgO oxide powders and the evolution of the amount of Fe^{2+} in the CNTs− Fe−MgO nanocomposite powders versus the urea ratio are consistent with the values of the MgO unit-cell parameters

Carbon Nanotubes by a CVD Method

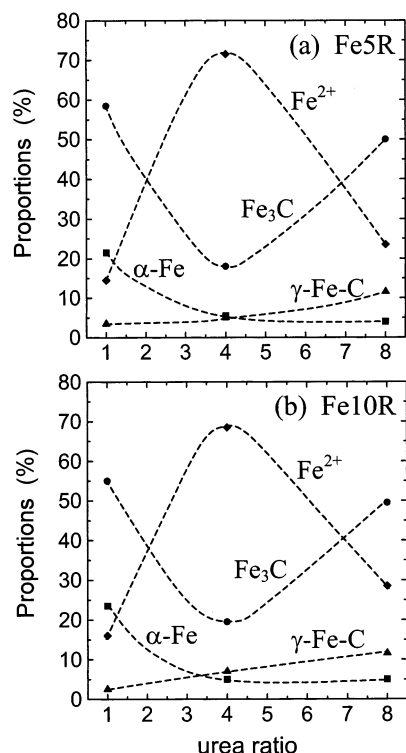*J. Phys. Chem. B, Vol. 106, No. 51, 2002* **13209**

Figure 12. Proportions of the RT Mössbauer components in the Fe5R (a) and Fe10R (b) nanocomposite powders versus the urea ratio used for the combustion of the corresponding oxide precursors (values from Table 3).

presented in Table 2. Several authors[34,39,45] have studied the reduction of $MgF_2O_4-Mg_{1-x}Fe_xO$ oxide mixtures in H_2. It appears that $MgFe_2O_4$-like particles are directly reduced to metallic iron whereas Fe^{3+} ions that are well dispersed in the O_h sites of MgO are first reduced to Fe^{2+} ions. The increase in the amount of Fe^{2+} upon reduction of the present Fe/MgO oxide powders at 1000 °C shows thus that the reduction rate of well-dispersed iron ions to metallic iron in these oxides is low. Carles et al.[46] have indeed shown that a 1-h reduction in H_2 at 1300 °C is necessary to reduce a $Mg_{0.9}Fe_{0.1}O$ solid solution fully. Previous works[4,14] indicated that the Fe_3C phase detected in the post-reduction analysis corresponds to particles on the surface of the matrix grains that are involved in the formation of the CNTs and the thick carbon nanofibers. The amount of Fe_3C is high in Fe10U1R, decreases steeply to reach a minimum in Fe10U4R, and then increases in Fe10U8R, where it is similar to the amount in Fe10U1R (Figure 12b). The low reduction yield of well-dispersed ions implies that Fe_3C results mainly from the reduction of Fe^{3+} clusters and $MgFe_2O_4$-like particles. Indeed, Fe10U1 consists mostly of highly agglomerated Fe^{3+} clusters and $MgFe_2O_4$-like particles,[20] which will give rise upon reduction to a large amount of Fe_3C, which tends to form large particles because of coalescence. This is reflected in the broad particle-size distribution of Figure 6a. Moreover, as illustrated in Figure 7, the particle size is directly correlated to the diameter of the carbon filaments. This suggests that most of the Fe_3C detected in Fe10U1R was involved in the formation of thick nanofibers, resulting in a rather low quantity of CNTs (Figure 1b) and the poor quality of the carbon (Figure 1c). In Fe10U4, the number of Fe^{3+} ions that form clusters decreases considerably,[20] giving rise to a strong decrease in the amount of Fe_3C-(Figure 12b), which is also reflected in the small CNTs quantity, as observed in Figure 1b. Some Fe^{3+} clusters in Fe10U4 are agglomerated and can form large particles upon reduction. However, Fe10U4 contains the highest number of well-dispersed

iron ions in MgO. A higher number of metallic particles resulting from the reduction of these ions can hence be expected in Fe10U4R. These particles will be smaller than those obtained from ion clusters. This appears in the particle-size distribution shown in Figure 6b, revealing a high proportion of small metallic particles (<5 nm) together with large particles similar to the ones in Fe10U1R (Figure 6a). A higher proportion of CNTs among the carbon species can therefore be expected, resulting in higher carbon quality as depicted in Figure 1c. In Fe10U8, the number of Fe^{3+} ions that form clusters and $MgFe_2O_4$-like particles is high,[20] resulting in a large amount of Fe_3C in Fe10U8R (Figure 12b). Moreover, the Fe^{3+} clusters and $MgFe_2O_4$-like particles are very well dispersed in Fe10U8 because of the large expansion of the powder. Coalescence upon reduction will be less effective, resulting in a larger number of particles with a size adequate for CNT formation (Figure 6c). This can explain the higher CNT quantity as observed in Figure 1b. The large $MgFe_2O_4$-like particles found for Fe10U8 will give rise to the thick nanofibers in Fe10U8R. However, such large particles as in Fe10U4R and Fe10U1R are not present in Fe10U8R (Figure 6), which is reflected in the higher carbon quality in the latter powder (Figure 1c).

γ-Fe−C is characteristic of small particles that are mostly dispersed inside the matrix grains.[4,14] Its concentration is low in Fe10U1R, which contains mainly large metallic particles, but increases in Fe10U4R and Fe10U8R (Figure 12b). In Fe10U4R, such small particles can be formed from well-dispersed ions in the MgO lattice of Fe10U4,[20] whereas in Fe10U8R they can result from the reduction of the very small Fe^{3+} clusters detected in Fe10U8.[20]

The α-Fe sextet concerns particles both inside the matrix grains (and thus relatively small) and outside the matrix grains, the latter being covered by carbon layers but being too large to be fully carburized.[4,14] It can also be assumed that the large metal species that partially fill the thick carbon nanofibers are either α-Fe or Fe_3C. The amount of α-Fe is consequently higher in Fe10U1R than in Fe10U4R and Fe10U8R (Figure 12b).

Conclusions

The aim of this paper was to study the formation of CNTs from different Fe/MgO oxide powders that were prepared by combustion synthesis and characterized in detail in a companion paper.[20] Powders containing different amounts of iron were investigated, but no major difference was found. Upon reduction during heating at 5 °C/min up to 1000 °C in H_2/CH_4 of the Fe/MgO oxide powders, the Fe^{3+} ions that are well dispersed in the O_h sites of MgO tend to form Fe^{2+} ions that are not likely to be reduced to metallic iron, whereas the $MgFe_2O_4$-like particles are directly reduced to metallic iron. The reduced phases are α-Fe, Fe_3C, and γ-Fe−C. Fe_3C appears to be the postreaction phase involved in the formation of carbon filaments (CNTs and thick nanofibers). The reduction of the Fe/MgO oxide powders prepared with a urea ratio of 1 produces large metal particles (<100 nm and average diameter of 32.1 nm) resulting from the coalescence of the poorly dispersed Fe^{3+} clusters and $MgFe_2O_4$-like particles. These particles are mostly involved in the formation of thick carbon nanofibers, the outer diameter of which is determined by the particle size. These nanofibers consist of poorly structured carbon and are hollow and partially filled with metal and/or carbide. For a urea ratio of 4, the reduction of the well-dispersed iron ions in the MgO lattice leads to small catalytic particles (<5 nm) that tend to form SWNTS and DWNTs with an inner diameter close to 2 nm. However, large particles (up to ∼60 nm in diameter) due

Coquay et al.

to the coalescence of Fe^{3+} clusters are responsible for the formation of thick carbon nanofibers, and 70% of the iron remains substituted in the MgO lattice. This results in a low CNT quantity and low carbon quality. For a urea ratio of 8, the reduction involves Fe^{3+} clusters and $MgFe_2O_4$-like particles that are well dispersed in the oxide powder. This results in the formation of small metal particles with a narrow size distribution. The formation of SWNTS and DWNTs with an inner diameter close to 2 nm prevails over that of nanofibers. The potential of nanometric $MgFe_2O_4$-like particles to form SWNTs and DWNTs constitutes a new result that may warrant further study. The results from the present work will be used to tailor oxide precursors for the formation of CNTs.

References and Notes

(1) Hafner, J. H.; Bronikowski, M. J.; Azamian, B. K.; Nikolaev, P.; Rinzler, A. G.; Colbert, D. T.; Smith, K. A.; Smalley, R. E. *Chem. Phys. Lett.* **1998**, *296*, 195.

(2) Flahaut, E.; Peigney, A.; Laurent, Ch.; Rousset, A. *J. Mater. Chem.* **2000**, *10*, 249.

(3) Bacsa, R. R.; Laurent, Ch.; Peigney, A.; Bacsa, W. S.; Vaugien, Th.; Rousset, A. *Chem. Phys. Lett.* **2000**, *323*, 566.

(4) Peigney, A.; Coquay, P.; Flahaut, E.; Vandenberghe, R. E.; De Grave, E.; Laurent, Ch. *J. Phys. Chem. B* **2001**, *105*, 9699.

(5) Herrera, J. E.; Balzano, L.; Borgna, A.; Alvarez, W. E.; Resasco, D. E. *J. Catal.* **2001**, *204*, 129.

(6) Alvarez, W. E.; Kitiyanan, B.; Borgna, A.; Resasco, D. E. *Carbon* **2001**, *39*, 547.

(7) Li, Y.; Liu, J.; Wang, Y.; Wang, Z. L. *Chem. Mater.* **2001**, *13*, 1008.

(8) Peigney, A.; Laurent, Ch.; Dobigeon, F.; Rousset, A. *J. Mater. Res.* **1997**, *12*, 613.

(9) Peigney, A.; Laurent, Ch.; Dumortier, O.; Rousset, A. *J. Eur. Ceram. Soc.* **1998**, *18*, 1995.

(10) Laurent, Ch.; Peigney, A.; Rousset, A. *J. Mater. Chem.* **1998**, *8*, 1263.

(11) Laurent, Ch.; Peigney, A.; Flahaut, E.; Rousset, A. *Mater. Res. Bull.* **2000**, *35*, 661.

(12) Quénard, O.; De Grave, E.; Laurent, Ch.; Rousset, A. *J. Mater. Chem.* **1997**, *7*, 2457.

(13) Govindaraj, A.; Flahaut, E.; Laurent, Ch.; Peigney, A.; Rousset, A.; Rao, C. N. R. *J. Mater. Res.* **1999**, *14*, 2567.

(14) Coquay, P.; De Grave, E.; Vandenberghe, R. E.; Dauwe, C.; Flahaut, E.; Laurent, Ch.; Peigney, A.; Rousset, A. *Acta Mater.* **2000**, *48*, 3015.

(15) Flahaut, E.; Govindaraj, A.; Peigney, A.; Laurent, Ch.; Rousset, A.; Rao, C. N. R. *Chem. Phys. Lett.* **1999**, *300*, 236.

(16) Kingsley, J. J.; Patil, K. C. *Mater. Lett.* **1988**, *6*, 427.

(17) Patil, K. C. *Bull. Mater. Sci.* **1993**, *16*, 533.

(18) Bacsa, R. R.; Laurent, Ch.; Peigney, A.; Vaugien, Th.; Flahaut, E.; Bacsa, W. S.; Rousset, A. *J. Am. Ceram. Soc.* **2002**, *85*, 2666.

(19) Coquay, P.; De Grave, E.; Peigney, A.; Vandenberghe, R. E.; Laurent, Ch. *J. Phys. Chem. B* **2002**, *106* 13186.

(20) Zhang, Y.; Stangle, G. C. *J. Mater. Res.* **1994**, *9*, 1997.

(21) Wagman, D. D.; Kilpatrick, J. E.; Taylor, W. J.; Pitzer, K. S.; Rossini, F. D. *J. Res. Natl. Bur. Stand. (U.S.)* **1945**, *34*, 143.

(22) Peigney, A.; Laurent, Ch.; Flahaut, E.; Bacsa, R. R.; Rousset, A. *Carbon* **2001**, *39*, 507.

(23) Dinnebier, R. E.; Eysel, W. Abstract of Powder Diffraction Satellite Meeting of the XVth Congress of the International Union of Crystallography, Toulouse, France, 1990; p 279.

(24) Holland, T. J. B.; Redfern, S. A. T. *Mineral. Mag.* **1997**, *61*, 65.

(25) Vandenberghe, R. E.; De Grave, E.; de Bakker, P. M. A. *Hyperfine Interact.* **1994**, *83*, 29.

(26) Dai, H.; Rinzler, A. G.; Nikolaev, P.; Thess, A.; Colbert, D. T.; Smalley, R. E. *Chem. Phys. Lett.* **1996**, *260*, 471.

(27) Kong, J.; Cassell, A. M.; Dai, H. *Chem. Phys. Lett.* **1998**, *292*, 567.

(28) Cassell, A. M.; Raymakers, J. A.; Kong, J.; Dai, H. *J. Phys. Chem. B* **1999**, *109*, 6484.

(29) Cheng, H. M.; Li, F.; Sun, X.; Brown, S. D. M.; Pimenta, A.; Marucci, A.; Dresselhaus, G.; Dresselhaus, M. S. *Chem. Phys. Lett.* **1998**, *289*, 602.

(30) Colomer, J. F.; Bister, G.; Willems, I.; Konya, Z.; Fonseca, A.; Van Tendeloo, G.; B.Nagy, J. *Chem. Commun.* **1999**, 1343.

(31) Li, Y.; Kim, W.; Zhang, Y.; Rolandi, M.; Wang, D.; Dai, H. *J. Phys. Chem. B* **2001**, *105*, 11424.

(32) Kitiyanan, B.; Alvarez, W. E.; Harwell, J. H.; Resasco, D. E. *Chem. Phys. Lett.* **2000**, *317*, 497.

(33) Su, M.; Zheng, B.; Liu, J. *Chem. Phys. Lett.* **2000**, *322*, 321.

(34) Boudart, M.; Delbouille, A.; Dumesic, J. A.; Khammouma, S.; Topsoe, H. *J. Catal.* **1975**, *37*, 486.

(35) Carles, V.; Rousset, A. *Solid State Ionics* **1996**, *83*, 309.

(36) Jing, J.; Campbell, S. J. *Hyperfine Interact.* **1991**, *68*, 283.

(37) Perez, A.; Marest, G.; Sawicka, B. D.; Sawicki, J. A.; Tyliszczak, T. *Phys. Rev. B* **1983**, *28*, 1227.

(38) Simkin, D. J.; Ficalora, P. J.; Bernheim, R. A. *Phys. Lett.* **1965**, *19*, 536.

(39) Topsoe, H.; Dumesic, J. A.; Derouane, E. G.; Clausen, B. S.; Morup, S.; Villadsen, J.; Topsoe, N. *Stud. Surf. Sci. Catalysis* **1979**, *3*, 365.

(40) Woods, K. N.; Fine, M. E. *J. Appl. Phys.* **1969**, *40*, 3425.

(41) Bodker, F.; Morup, S. *Hyperfine Interact.* **1994**, *93*, 1421.

(42) Hayashi, M.; Tamura, I.; Fukano, Y.; Kanamaki, S. *Phys. Lett. A* **1980**, *77*, 332.

(43) Yakel, H. L. *Int. Met. Rev.* **1985**, *30*, 17.

(44) Bi, X. X.; Ganguly, B.; Huffman, G. P.; Huggins, F. E.; Endo, M.; Eklund, P. C. *J. Mater. Res.* **1993**, *8*, 1666.

(45) Bhide, V. G.; Tambe, B. R. *J. Mater. Sci.* **1969**, *4*, 955.

(46) Carles, V.; Brieu, M.; Demai, J. J.; Rousset, A. In *Euro-Ceramics*, 4th ed.; Galassi, C., Ed.; Gruppo Editoriale Faenza Editrice S. p. A.: Faenza, Italy, 1995; Vol. 1, p 323.